# Observation of horizontal temperature variations by a spatial heterodyne interferometer using single-sided interferograms

Konstantin Ntokas[1], Jörn Ungermann[1], Martin Kaufmann[1], Tom Neubert[2], and Martin Riese[1]

[1]Institute of Energy and Climate Research (IEK-7: Stratosphere), Forschungszentrum Jülich, Jülich, Germany
[2]Central Institute of Engineering, Electronics and Analytics (ZEA-2: Electronic Systems), Forschungszentrum Jülich, Jülich, Germany

**Correspondence:** Konstantin Ntokas (k.ntokas@fz-juelich.de)

**Abstract.** Analyses of the mesosphere and lower thermosphere suffer from a lack of global measurements. This is problematic because this region has a complex dynamic structure, with gravity waves playing an important role. A limb sounding spatial heterodyne interferometer (SHI) was developed to obtain atmospheric temperature retrieved from the $O_2$ A-band emission, which can be used to derive gravity wave parameters in this region. The 2-D spatial distribution of the atmospheric scene is captured by a focal plane array. The SHI superimposes the spectral information onto the horizontal axis across the line-of-sight (LOS). In the usual case, the instrument exploits the horizontal axis to obtain spectral information and uses the vertical axis to get spatial information, i.e. temperature observations at the corresponding tangent points. This results in a finely resolved 1-D vertical atmospheric temperature profile. However, this method does not make use of the horizontal across LOS information contained in the data.

In this manuscript a new processing method is investigated, which uses single-sided interferograms to gain horizontal across LOS information of the observed temperature field. Hereby, the interferogram is split and each side is mirrored at the center of the horizontal axis. Each side can then be used to retrieve an individual 1-D temperature profile. The location of the two retrieved temperature profiles is analysed using prescribed horizontal temperature variations, as it is needed for deriving wave parameters. We show that it is feasible to derive two independent temperature profiles, which however will increase the requirements of an accurate calibration and processing.

## 1  Introduction

The dynamical structure of the mesosphere and lower thermosphere (MLT) is mainly driven by atmospheric waves like planetary waves, tides and gravity waves (Vincent, 2015). Gravity waves are small to medium scale wave patterns, which transport energy from lower altitudes to the MLT region. Commonly known sources of gravity waves in the lower atmosphere are the uplift of air masses due to orography, convection, and unstable jets. Alexander et al. (2010) summarized the current treatment of gravity waves in global circulation models, where unresolved gravity waves are mostly parameterized. Becker and Vadas (2020) pointed out that gravity waves can also have sources in higher altitudes which are not well understood, but can have a large effect on the MLT region. Chen et al. (2022) underlined the importance of gravity wave observations by multiple examples and outlined an observation method where gravity wave parameters can be extracted from temperature fields.

25     Temperature in the MLT region can be derived by measuring the $O_2(0,0)$ atmospheric A-band emissions at 762nm as shown by Ortland et al. (1998) and Sheese (2009). The same atmospheric band was used by the Michelson Interferometer for Global High-resolution Thermospheric Imaging (MIGHTI) instrument aboard the NASA Ionospheric Connection Explorer (ICON) mission (Englert et al., 2017). MIGHTI uses three narrow band regions within the oxygen A-band to derive the temperature product. Notably, large-scale gravity waves have been detected through measurements taken in 2020, as reported by Triplett

30 et al. (2023). Additionally, the Swedish MATS (Mesospheric Airglow/Aerosol Tomography and Spectroscopy) satellite mission employs two band regions within the oxygen A-band to extract temperature information, and the potential application of this data for gravity wave observations is explored in a simulation study by Gumbel et al. (2020). Both MIGHTI and MATS employ multichannel photometric measurements.

    Simultaneously, a collaborative effort between the Jülich Research Center and the University of Wuppertal in Germany led

35 to the development of a limb sounding ~~instrument (Kaufmann et al., 2018)~~spatial heterodyne interferometer (SHI) for deriving temperature in the MLT from the oxygen A-band emission (Kaufmann et al., 2018; Song et al., 2017). This instrument ~~has the capability to resolve the separate~~ employs interferometry, enabling the resolution of individual emissions within the oxygen A-band~~by using interferometry. Furthermore,~~. After a successful in-orbit demonstration of the measurement technology in 2018, an improved second version, called AtmoLITE, was developed and built for the International Satellite Program in Research and

40 Education (INSPIRE). Additionally, the European Commission has selected this instrument for in-orbit validation as part of its H2020 program. Details of the AtmoLITE instrument design are partially covered by Chen et al. (2022) and will be described further in Sec. 2 and Sec. 3.1.

    The temperature is derived from ~~the instrument design incorporates a vertical resolution of , enabling it to effectively capture and analyze small to medium-scale vertically propagating gravity waves.The temperature can be derived from~~ relative inten-

45 sities of the $O_2(0,0)$ atmospheric A-band emission lines. ~~Thus~~Consequently, no absolute radiometric calibration is ~~needed, which facilitates the calibration of the instrument. The emission is visible~~ required, simplifying the calibration process. Notably, these emissions are visible both during day- and night-time. The instrument is highly miniaturized and energy efficient so that it can fly on nanosatellites, so called CubeSats (Poghosyan and Golkar, 2017). CubeSats allow a cost-efficient way to design and operate satellites due to the utilization of largely standardized components. ~~After a successful in-orbit demonstration of~~

50 ~~the measurement technology in 2018, an improved second version has been developed in the recent years for the International Satellite Program in Research and Education (INSPIRE). Furthermore, the European Commission has selected the instrument for an in-orbit validation to demonstrate innovative space technologies within its H2020 program. The current instrument design is partly described by Chen et al. (2022) and will be described further in Sec. 2 and Sec. 3.1.~~

~~Our~~ The AtmoLITE instrument works as a camera where the atmospheric scene is mapped onto the detector. ~~A spatial~~

55 ~~heterodyne interferometer (SHI ) is used to detect the spectrum~~ The SHI superimposes the spectral information of the $O_2$ A-band emission ~~and superimposes the spectral information~~ in horizontal direction across the LOS. Each image thus contains superimposed spectral and spatial information along the horizontal axis while preserving spatial information vertically. In the usual processing, ~~the horizontal direction is used to extract spectral information and vertical direction gives spatial information. This allows to extract a~~ spectral information is extracted from the horizontal axis, and spatial information is derived from the

60 vertical axis. This approach enables the extraction of finely resolved 1-D temperature ~~profile from one image, which can be subsequently~~ profiles with an intended vertical resolution of 1.5km from a single image. The resulting temperature profiles can then be used to derive wave parameters~~as described~~, as outlined by Ern (2004) and ~~applied for our~~ adapted for the AtmoLITE instrument by Chen et al. (2022). This capability allows AtmoLITE to effectively capture and analyze vertically propagating gravity waves of small to medium-scale.

To exploit some of the spatial information in horizontal direction, we propose a new processing method which allows to retrieve two 1-D temperature profiles from one image by using single sided interferograms and mirroring them at the center. Johnson et al. (1996) and Gisi et al. (2012) already used mirrored interferograms for the far-infrared spectrometer (FIRS)-2 and for the TCCON FTIR spectrometer, respectively, to achieve a higher spectral resolution. In our case, we use the single-sided interferogram to gain horizontal information of the measured atmospheric scene. Chen et al. (2022) showed in a simulation
70 study that medium-scale gravity waves can be resolved, if it is possible to obtain two temperature profiles from a single interferogram. The methodology to fulfill this requirement is described in this paper.

A thorough precision analysis is key to assess the limitations of this method. Therefore we detail the precision budget of the data product, in particular with regard to signal-to-noise limitations at the upper boundary of the measurement domain.

The paper is structured as follows. We introduce the instrument in Sec. 2. An overview of the simulation setup is given in
75 Sec. 3, containing the interferogram simulation presented in Sec. 3.1, followed by the detailed forward simulation in Sec. 3.2 and the data processing in Sec. 3.3. The temperature dependency of the emission lines and the resulting temperature precision are discussed in Sec. 4. An extended discussion on using half interferograms is given in Sec. 5. Hereby, we look at the temperature sensitivity of the retrieval with respect to the temperature variation in horizontal direction in Sec. 5.1. Further, we assess the locations of the retrieved temperatures using half interferograms for simulated horizontal temperature variations
80 in Sec. 5.2. At last we assess the effect of apodization onto the retrieval using half interferograms in Sec. 5.3.

## 2 Spatial heterodyne interferometer

A spatial heterodyne interferometer (SHI) is similar to a Michelson interferometer, but the two mirrors are replaced by fixed tilted gratings. This measurement method was firstly developed by Connes (1958) and with the subsequent availability of imaging detectors, it was further developed to remote sensing methods by e.g. Harlander et al. (1992), Cardon et al. (2003),
85 Watchorn et al. (2001). Figure 1 shows a schematic of the instrument. The incident light is imaged by the front optics onto diffraction gratings, after passing through a beam splitter. The camera optics images the gratings onto a 2-dimensional focal plane array (FPA). The tilt angle of the wave fronts and therefore the frequency of the interference pattern on the FPA is dependent on the frequency of the incoming light. Multiple emission lines result in superimposed cosine waves across the FPA in x-direction. The FPA is two dimensional, so that the spatial distribution of the atmospheric scene is maintained throughout
90 the instrument. One measurement therefore contains spatial information along the z-axis and superimposed spectral and spatial information along the x-axis. Note that the z- and x-axis correspond to the vertical and horizontal across-track dimension in the atmosphere.
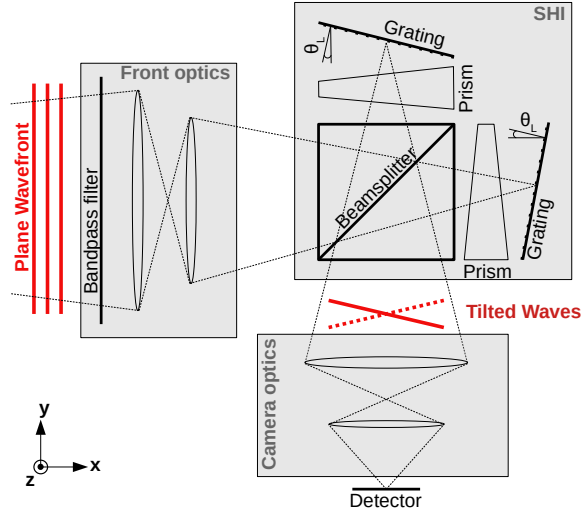
**Figure 1.** Schematic of the ~~SHS~~ SHI instrument

## 3 Simulation setup

An interferogram simulation is presented in Sec 3.1. The details of the forward simulation to calculate the expected signal is introduced in Sec. 3.2. At last the data processing is described in Sec. 3.3.

### 3.1 Interferogram simulation

The mathematical derivation for an interferogram measured by an SHI is presented by Harlander et al. (1992), Smith and Harlander (1999), and Cooke et al. (1999). Chen et al. (2022) give more details on the mathematics for the instrument described here.

A line-by-line model is used to simulate spectra which are converted to interferograms. A 1-D interferogram with some horizontal variation is defined by

$$I(x) = \sum_{i=1}^{I} S_i(x) \left[1 + \cos(2\pi f_i x)\right], \tag{1}$$

where $S_i(x)$ is the radiance variation across the horizontal field of view and $f_i$ is the spatial frequency for a given emission line $i$. The spatial frequency corresponds to the wavenumber by $f_i = 4(\sigma_i - \sigma_L)\tan\theta_L M$, where $\sigma_L$ and $\theta_L$ are the Littrow wavenumber and Littrow angle, respectively. The Littrow angle is the tilt of the gratings as shown in Fig. 1. Note, that the Littrow wavenumber corresponds to zero spatial frequency. $M$ is the magnification factor of the camera optics and $\sigma_i$ is the wavenumber of the emission line. This instrument uses a CMOS based detector, where shot noise dominates the precision of the data (Liu et al., 2019). Shot noise can be described by a Poisson process with mean and variance equal to the signal. For

**Table 1.** Summary of instrument specification

| Parameter | Property |
| --- | --- |
| Littrow wavenumber | $13047 \text{cm}^{-1}$ |
| Littrow angle | $6.6°$ |
| Magnification factor of camera optics | 0.57 |
| Groove density of gratings | $300 \text{mm}^{-1}$ |
| Spectral range | $13059 \text{cm}^{-1}$ to $13166 \text{cm}^{-1}$ |
| Field of view | $1.3 \text{deg}^2$ |
| | ($\approx 60 \text{km}^2$ for orbit altitude of 600km) |
| Etendue | $0.018 \text{cm}^2$ sr |
| Grating efficiency | 0.8 at 762nm |
| Detector | GSENSE400BSI |
| Detector number range | $0 - 4095$ (12bit) |
| Detector columns/rows | 860/860 |
| Pixel pitch | 11µm |
| Quantum efficiency | 0.7 at 762nm |

the expected signal levels, this can be approximated by an additive white Gaussian noise with standard deviation equal to the
110    square root of the signal in each pixel. The specification of the current instrument version is given in Tab. 1.

### 3.2   Detailed forward simulation

This section introduces shortly the simulation of the $O_2$ A-band emission, which is described by Chen et al. (2022) in detail. The
$O_2$ A-band is an electronic transition from the excited state $O_2(b^1\Sigma_g^+, v = 0)$ to the ground state $O_2(X^3\Sigma_g^-, v = 0)$ centered
at 762nm in the near-infrared. The band consists of multiple emission lines due to the transition of multiple rotational states~~,~~
115    ~~where absorptions and emissions~~. In order to calculate the emission energies between the rotational states~~are calculated using~~
~~,~~ the HITRAN database can be used (Gordon et al., 2022). The photo-chemical processes producing the excited ~~$O_2$~~ $O_2(^1\Sigma)$
molecules can be put in three groups. The first group is the absorption in the B-band and the A-band itself. The second group
produces excited ~~$O_2$~~ $O_2(^1\Sigma)$ molecules via collisional energy transfer with highly excited molecules and atoms produced by
photolysis of $O_2$ and $O_3$. The third is called Barth-process and is a purely chemical source, which was first described by Barth
120    and Hildebrandt (1961). It is independent of solar radiation and it is therefore the only process active during night-time. A
detailed description of the dayglow $O_2$ A-band excitation is given by Sheese (2009), Bucholtz et al. (1986), Zarboo et al.
(2018) and Yankovsky and Vorobeva (2020).

To calculate the $O_2$ A-band ~~emission~~ volume emission rates, data of the HAMMONIA (Hamburg Model for the Neutral and
Ionized Atmosphere) run of Schmidt et al. (2006) is used. It gives monthly averaged 3-D data sets for temperature, pressure
125    and the volume mixing ratios of the required substitutes involved in the photo-chemical processes for solar minimum and
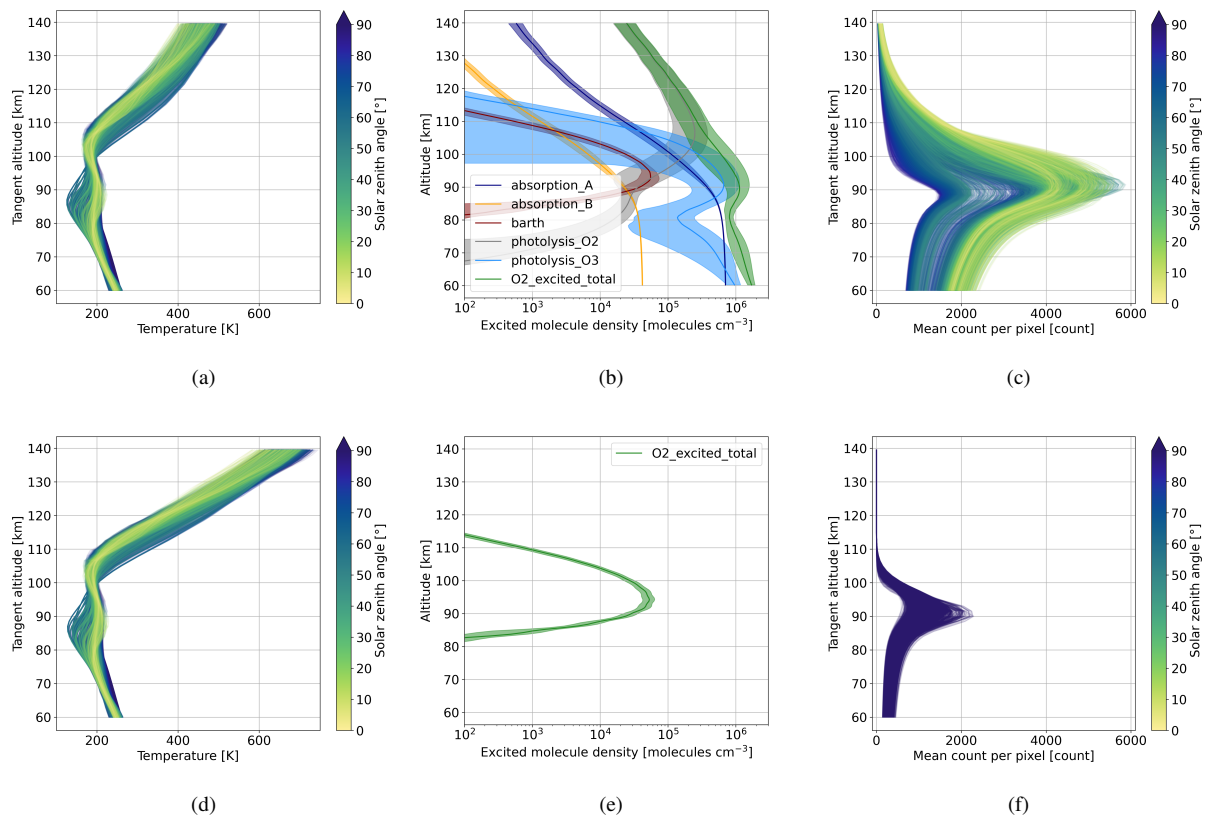
**Figure 2.** (a) and (d) 1-D input temperature profiles used in the forward calculation for solar minimum and maximum conditions, respectively; (b) number density of excited $O_2$ molecules due to the five production mechanisms during day-time condition; total excited $O_2$ is the sum of the five parts; (e) number density of excited $O_2$ molecules during night-time condition, where only the Barth process is active; (c) and (f) estimated count per pixel received at the detector during day- and night-time simulation, where the integration time is set to 1s and 10s, respectively; HAMMONIA data set is used for the forward simulations (Schmidt et al., 2006)

maximum conditions. The overall description of the used one-dimensional radiative transfer model is described by Chen et al. (2022). The model is used to generate test data sets to be used in the following study, covering a equidistant longitude and latitude grid of $10°$. At each longitude and latitude point the solar zenith angle is calculated by assigning the timestamp to noon at the 15th of each month. This is done for each month and for solar minimum and maximum conditions. The expected mean

130  signal per pixel at the detector can be calculated by

$$S_p(z) = \frac{S_r(z) \, E \, L \, t_{int}}{N} \tag{2}$$

where $S_r$ is the spectrally integrated radiation within the spectral range of the instrument for a given tangent altitude $z$, $E$ the etendue of the instrument, $L$ the loss factor or efficiency of the instrument (28% including grating efficiency, quantum

efficiency of the detector and loss of 50% due to the beam splitter), $t_{int}$ the integration time and $N$ is the total number of pixels of the 2d detector array. Figure 2a and Figure 2d display the input temperature profiles for solar minimum and solar maximum conditions, respectively. The figures illustrate noticeable temperature deviations above 120km between the two groups. Based on the temperature profiles, Figure 2b and Figure 2e show the mean and standard deviation of the expected number density of excited $O_2$ molecules due to the different production mechanisms for day- and night-time simulations, respectively. It should be noted that the Barth-process is the only active process during night-time conditions. Propagating this through the radiative transfer model and applying Eq. (2), where we assume 1s and 10s for day- and night-time, we can calculate the average count per pixel measured by the detector. The results are shown in Figure 2c and Figure 2f for day- and night-time simulations. The night-time simulations show a lower variability than the day-time simulations. This can be explained by the larger variation of the photolysis production mechanisms shown in Figure 2b, which is mainly caused by the varying solar zenith angle. Note that during day-time the expected signal at the instrument decreases below 90km which can be partly explained by the decreasing number density of excited $O_2$ in Figure 2b. However, for tangent altitudes below 85km self-absorption plays a major role, leading to a further decrease in the signal at the instrument despite the increase in the number density of excited $O_2$. This constrains the information content of temperature data obtained from measurements of that region. The decreasing signal in higher altitudes above 120km constraints the measurement method from above. Further discussion on the upper limit is given in Sec. 4. To neglect self-absorption in this paper, we will focus on a field of view between 80km and 140km. Consequently due to self-absorption effect, the results for the lowermost tangent altitudes, below $\approx$ 85km, need to be treated with reservation.

### 3.3 Fast data processing

The first step in the data processing is to subtract the non-modulated part, which corresponds to the low frequencies in the spectrum. Subsequently applying a Fourier transformation along the x-axis, the interferogram is converted into a spectrum. A 2-dimensional radiative transfer model is used to simulate across-track temperature variations. Assuming that self-absorption is small, we can focus on the area close to the tangent layer, where most of the information comes from when integrating along the line of sight. Note that this holds true for tangent altitudes above 85km for the $O_2$ A-band emission. Furthermore, stray light isn't included in this study, but it impacts day-time simulations, mainly tangent altitudes below 85km due to upwelling radiation and above 120km due to the low signal strength. A first assessment is presented by Kaufmann et al. (2023), and possible correction methods will be investigated in future research.

Since self-absorption is not considered in this study, a simplified forward model can be used to solve the inverse problem and retrieve temperature. Instead of calculating the full radiative transfer equation, it ~~takes the HITRAN data set to get~~ calculates the relative distribution of the oxygen A-band emission lines for a given temperature ~~,~~ following Song et al. (2017), where the required spectroscopic parameters of the emission lines are taken from the HITRAN data set. Subsequently, it convolves the emissions with a given instrument line shape (ILS) and scales the total spectrum with a scaling factor to match the output spectrum from the Fourier transform. In this context, the factor corresponds to the number density of excited $O_2(^1\Sigma)$ molecules. It is important to highlight that the atmospheric emission lines are very narrow, allowing to approximate them as shifted Dirac delta distributions. When a function is convolved with a Dirac impulse, the result is the same function shifted by an amount
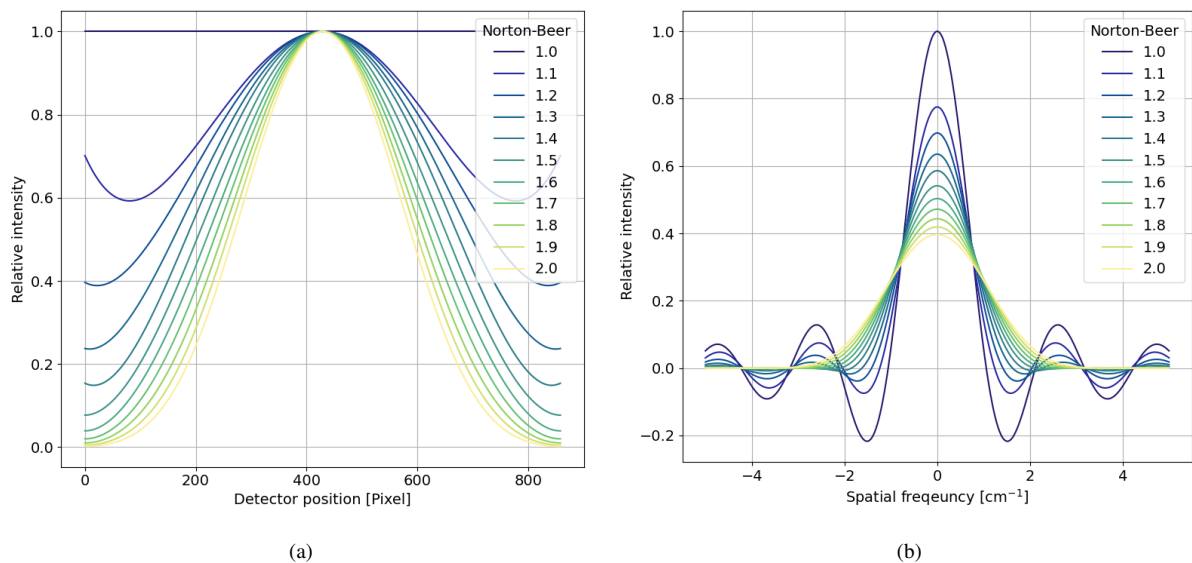
**Figure 3.** Apodization functions used for the assessment; (a) apodization function in the spatial domain; (b) apodization function in the spectral domain;

equal to the shift of the Dirac impulse. Consequently, the ILS can be positioned at the location of the emission line, scaled by the line strength and summed up to obtain an analytical spectrum for a given temperature. By employing this approach in the retrieval process, we can effectively derive an averaged temperature from the horizontal temperature variation for a given tangent altitude.

The ILS of a finite interferogram is defined by a sinc-function whose resolution is determined by the length of the interferogram. To minimize the side lobes of the sinc function, apodization is commonly applied in Fourier spectrometry resulting in a smoother spectral output. It increases the localization of the spectral information, which can also help to be more robust against instrumental errors. However, apodization decreases the spectral resolution and it is therefore a trade off between spectral resolution and decrease of the side lobes. Filler (1964) introduced the Filler's diagram, which plots these two measures against each other. It is often used to assess the performance of given apodization functions. Norton and Beer (1976) and Naylor and Tahic (2007) showed that the Norton-Beer apodization has the best properties. The extended version given by Naylor and Tahic (2007) is shown in Figure 3 for the spatial and spectral domain. 1.0 refers to no apodization, and 1.2, 1.4 and 1.6 refer to the weak, medium and strong apodization given by Norton and Beer (1976). Note that the number refers to the full width half maximum (FWHM) of the apodization function relative to the sinc function and thus higher number means stronger apodization.

(a)
(b)
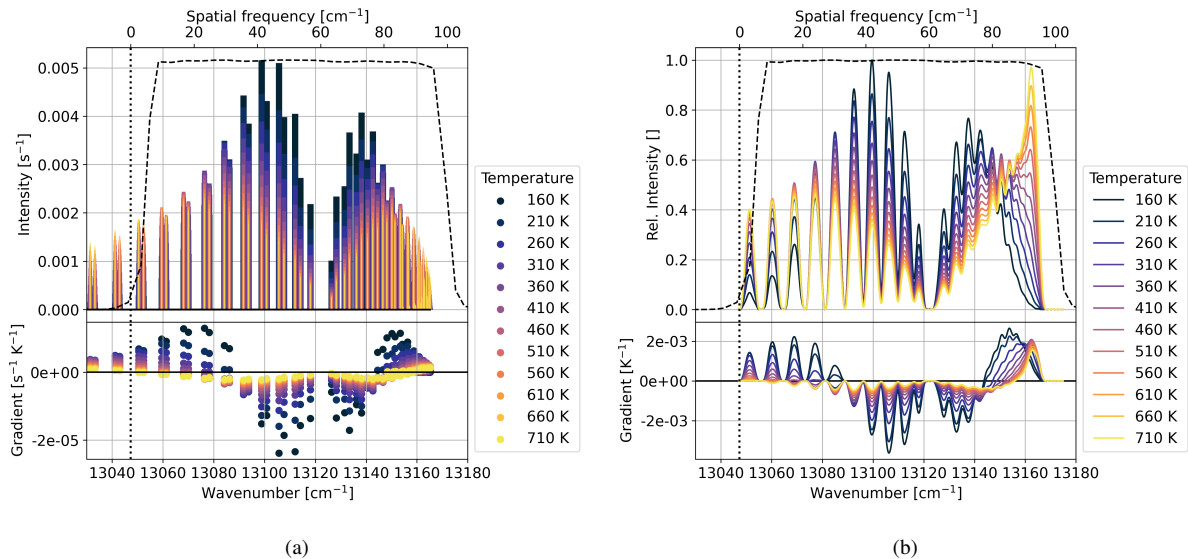
**Figure 4.** Rotational distribution of the $O_2$ A-band emission; the dashed and vertical dotted line indicate the curve of the bandpass filter and the Littrow wavenumber, respectively; the top x-axis shows the spatial frequency at the detector; the gradient is calculated by finite difference along the temperature axis; (a) Intensity of emission lines calculated using HITRAN for different temperatures; (b) convolution of emission lines with Norton-Beer strong ILS;

## 4 Temperature dependency of the $O_2$ A-band emission

Our simplified forward model relies on the temperature dependent rotational distribution of the $O_2$ A-band emission. The temperature dependency is shown in Figure 4a. At low temperatures the central frequencies show higher intensities, which decrease to the sides. Higher temperatures show a more broadened distribution which entails a decrease of the integrated intensity within the bandpass filter. The gradient with respect to temperature decreases with higher temperatures, which entails a decrease in sensitivity towards higher temperatures. Convolving the emission lines with an instrument line shape (ILS) corresponding to a Norton-Beer strong apodization (Sec. 3.3), results in the spectra presented in Figure 4b. Note the increase of the intensities at $13165 \mathrm{cm}^{-1}$ due to the high density of emission lines in the R-branch.

In the following, we propagate the shot noise in the interferogram through the simplified temperature retrieval for different signal levels and constant temperatures. For each signal level and temperature, we perform a Monte-Carlo simulation with 300 samples, simulate an ideal interferogram using Eq. (1) for a given signal level and temperature, apply shot noise approximated by additive white Gaussian noise with variance equal to the signal level, and retrieve temperature as presented in Sec. 3.3. The signal level is expressed in the signal-to-noise ratio (SNR), which is the ratio of the mean to the standard deviation thus the square root of the signal level itself. Figure 5 shows the bias and the standard deviation of the retrieved temperatures obtained in the Monte-Carlo simulations. The top axis shows the mean signal assuming that 20 rows are accumulated, which increases the SNR by a factor of $\sqrt{20}$. The main reason for the binning is the limited data downlink capacity of micro-satellites. A binning
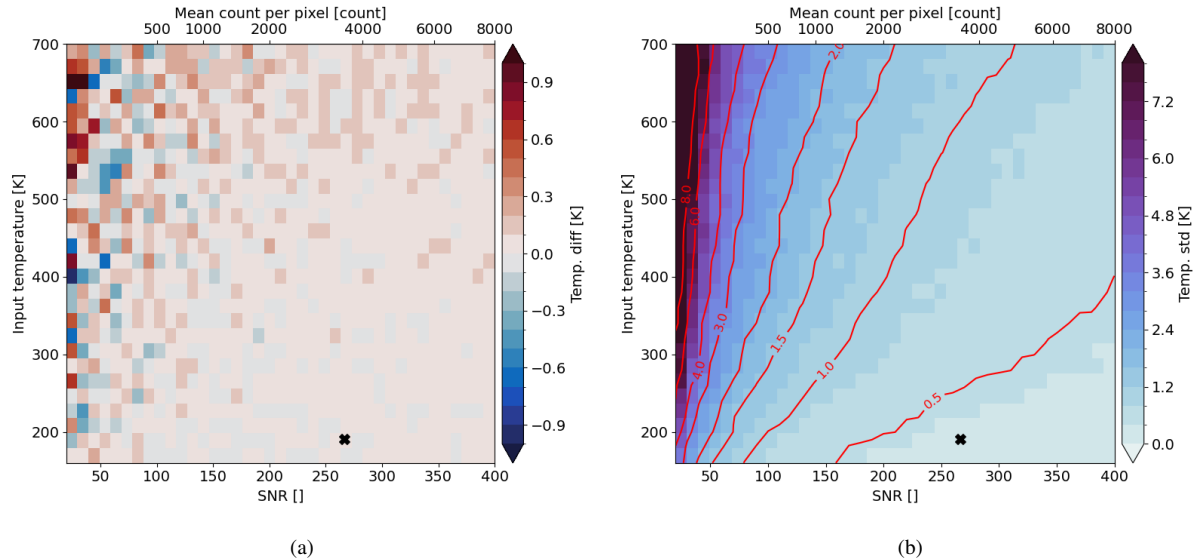
**Figure 5.** Results of the Monte-Carlo simulations with 300 samples where shot noise is propagated into the temperature retrieval for different SNRs and temperatures; (a) mean temperature differences; (b) standard deviation of the retrieved temperatures; contour lines are calculated on smoothed data; the marker indicate the mean expected SNR and temperature in the mesopause region at 90km altitude

of 20 rows results in a vertical spatial sampling of approximately $1.5$km. The lower sensitivity of the the the $O_2$ A-band emission
200   with higher temperatures is also here visible. For higher temperature either a higher SNR is needed to keep the precision at the same level, or one needs to accept a lower precision if SNR stays constant. The bias for low signals in Figure 5a is caused by using magnitudinal spectra. When taking the the absolute value of the spectrum, the spectral noise follows a Rice distribution (Talukdar and Lawing, 1991) which deviates from the normal distribution for spectral values close to zero. Therefore, low signals are affected more. More details on the spectral noise of a magnitudinal spectrum is given in Appx. A.

205   We then evaluate the interpolated temperature precision field presented in Figure 5b on the expected signal levels (Figure 2c and 2f) for typical temperature profiles in the MLT region (Figure 2a and 2d). Hereby, we assume a binning of 20 rows. The results are shown in Figure 6. The night-time simulation gives an temperature precision below $1$K for tangent altitudes between $85$km and $100$km. For the day-time simulation, a temperature precision of around $0.5$K can be achieved in the strong signal layer between $85$km and $95$km. The temperature precision then decreases for higher tangent altitudes due to the decrease in
210   signal and higher temperatures.

  In the next step, we assess the required number of binning rows to achieve a certain temperature precision. Hereby, we extract a contour line from the temperature precision field in Figure 5b, get the required signal for the temperatures presented in Figure 2a and 2d and calculate the required binning using the expected signal in Figure 2c and 2f for day- and night-time simulations, respectively. The results for different temperature precision levels are shown in Figure 7. During day-time we
215   expect to resolve the higher altitudes on average up to approximately $105$km, $115$km, $125$km and $135$km with a temperature

(a)                                                                                          (b)
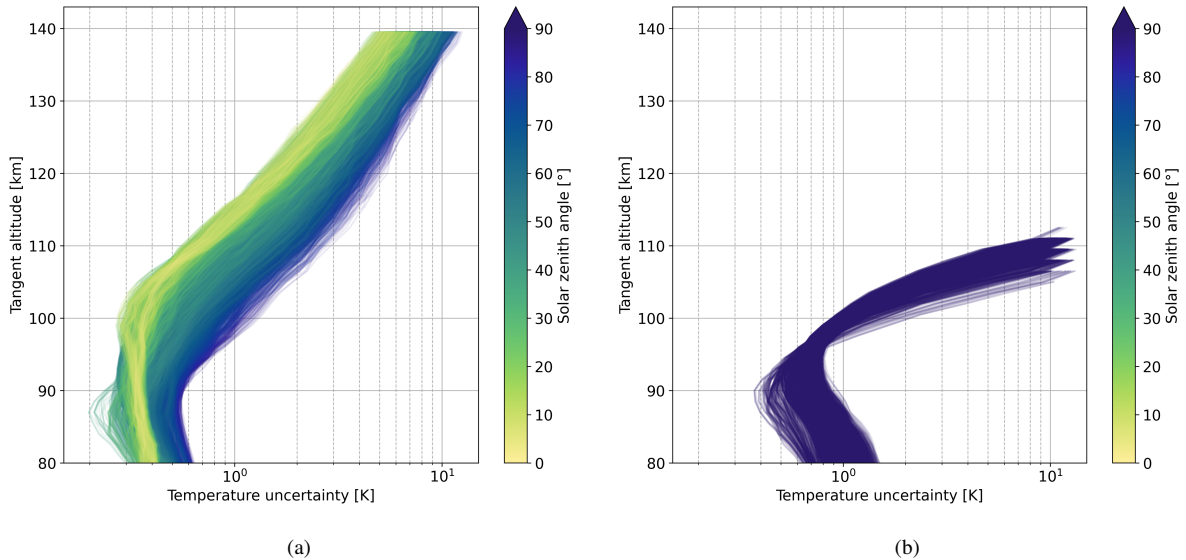
**Figure 6.** Temperature precision calculated from the expected signal and input temperature presented in Figure 2 and using an interpolated temperature precision field presented in Figure 5b assuming a binning of 20 rows; (a) and (b) depict the day- and night-time conditions, respectively; note that signal counts below 100 counts are not considered which cuts off the night-time simulations around 110km

precision of 1K, 2K, 4K and 8K, respectively, when a binning of 20 rows is applied. During night-time simulation, accepting low temperature precision does not help to resolve higher altitudes because the signal decreases strongly above 100km, as shown in Figure 2f. In general, a larger binning can be applied to get more accurate results at the cost of spatial resolution, which is already proposed by Florczak et al. (2022). It is therefore a trade-off between spatial sampling and temperature precision.

## 5   Obtaining horizontal spatial information by interferogram splitting

As explained in Sec. 2, the instrument contains the 2-D spatial distribution of temperature in its field of view. To gain more information, one can split the interferogram at the zero optical path difference (ZOPD). Exploiting the symmetry of the interferogram, each side is then mirrored around the ZOPD. This results in an interferogram of equal length as using the full interferogram, which then entails the same spectral resolution. When using the full interferogram, one half of the shot noise propagates into the real and the other half into the imaginary part of the spectrum. Mirroring the interferogram however causes the shot noise to be symmetric, so that it is then fully propagated into the real part of the spectrum, resulting in a higher noise level by a factor of $\sqrt{2}$. To show this numerically, we perform a Monte-Carlo simulation with 300 samples, where we simulate an interferogram using Eq. (1) for a constant temperature of 200K across the horizontal field of view. The signal level is set to a SNR of 100, which results in a temperature precision of approximately 1K as seen in Figure 5b. Figure 8a shows the mean
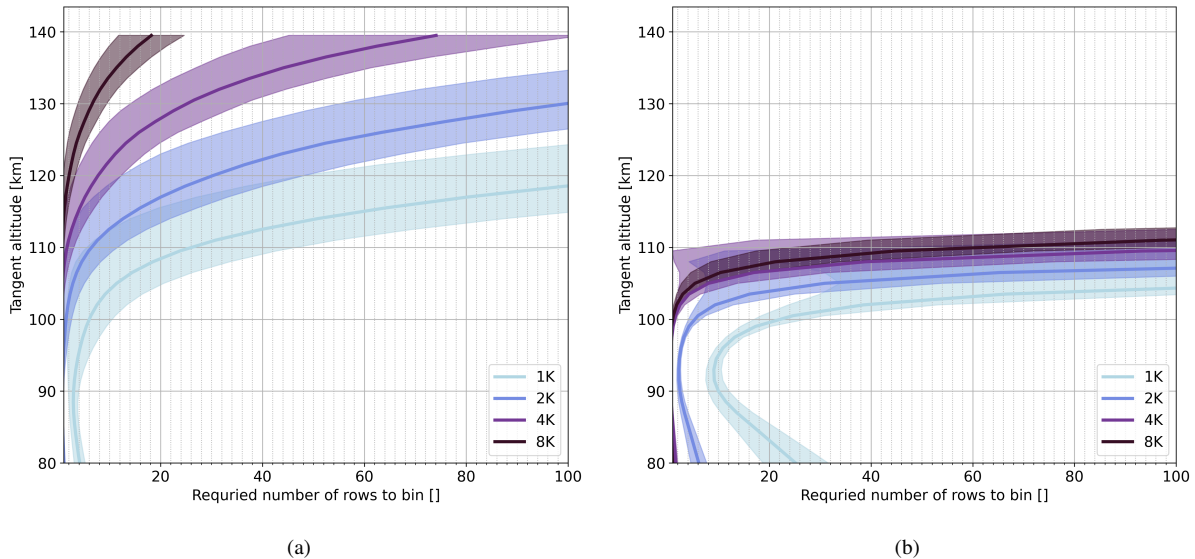
**Figure 7.** Required binning of rows to achieve a certain temperature precision (a) during day-time and (b) during night-time; the solid line shows the mean and the shaded area the standard deviation of all used samples from Figure 2c and 2f

and the standard deviation of the interferogram samples. In the following step, we run through the processing chain explained in Sec. 3.3, extract the spectral noise and retrieve the temperature for each Monte-Carlo sample. The results are shown in Figure 8b. As a reference we show the spectrum without noise. Further, we show the standard deviation of the noise of the 300 samples for the case using the full interferogram and the two cases using mirrored single-sided interferograms. As stated be-

235 fore, the noise level is higher by a factor of $\sqrt{2}$ for the mirrored single-sided interferograms compared to the full interferogram. This results in a correspondingly increased temperature precision of $1.4$K. Note that normally the noise is evenly distributed in the spectrum. If the signal however is close to zero, the noisy signal can take positive and negative values. Considering only magnitudinal spectra, the negative values are mirrored, resulting in a smaller standard deviation. More discussion on this is given in Appx. A.

240 Performing the same analysis for multiple SNR and temperature levels gives the temperature precision of the right single-sided interferograms depicted in Figure 9a. Figure 9b shows that for most temperature and SNR levels it holds true that the temperature precision is decreased by a factor of $\sqrt{2}$ when using only the right single-sided interferogram. The same simulation has been performed for the left single-sided interferogram and showed a similar result. Thus, we can conclude that the increase of spectral noise by a factor of $\sqrt{2}$ results in a decreases temperature precision by the same factor.

245 To study the influence of horizontal temperature variation on the temperature retrieval, we look at a simple example first. A linear temperature gradient of 20K over the horizontal field of view of 60km, shown in Figure 10a, is incorporated into the interferogram by using Eq. (1). Figure 4a shows that for higher temperatures the integrated intensity within the bandpass filter decreases as the distribution of the emission lines becomes flatter. Following Eq. (1), the interferogram is just the sum of cosine

(a)  (b)
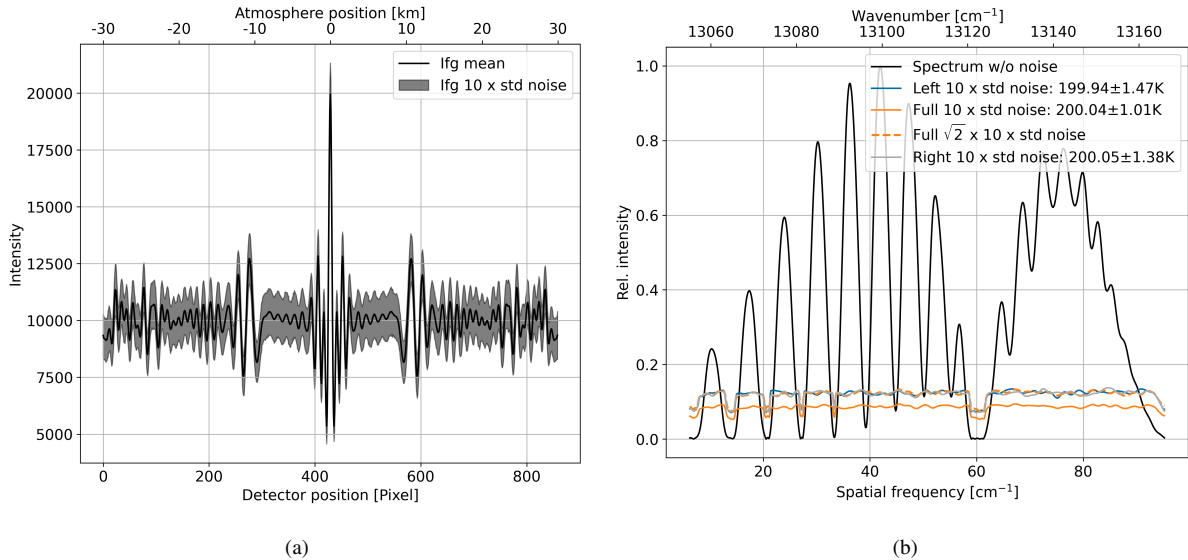
**Figure 8.** Results of Monte-Carlo simulations with 300 samples where shot noise is propagated through the spectrum into the temperature retrieval for an interferogram with a constant temperature of 200K; (a) mean and $10\times$ the standard deviation of the 300 interferogram samples; (b) spectrum without noise as a reference; $10\times$ the standard deviation of the spectral noise using full interferograms and left- and right-side of the interferograms; standard deviation of the noise using the full interferograms multiplied by a factor of $\sqrt{2}$ is shown as dashed line; Norton-Beer strong apodization is applied;

waves with amplitude and offset equal to the intensity of the emission lines. The interferogram's baseline therefore also shows
250   a decrease with higher temperatures, as shown in Figure 10b. It shows an interferogram without noise and without temperature
gradient as reference. We also show the difference between the interferogram with the linear temperature gradient and the
reference interferogram relative to the mean signal of the reference interferogram. The linear regression of the difference agrees
well with the relative variation of the integrated intensity within the bandpass filter. We perform a Monte-Carlo simulation
with 300 samples with shot noise modelled in the interferogram space. We run through the processing chain as explained
255   in Sec. 3.3 to get a spectrum and a retrieved temperature for each sample. Note that the temperature gradient results in a
tilted non-modulated part which is fitted and subtracted before splitting the interferogram. This is performed for the case
using the full interferogram as well as the left and right mirrored interferogram, separately. Figure 10c shows the mean of
all noisy spectra with constant temperature gradient as a reference. Furthermore, the smoothed mean difference of the noisy
spectra incorporating the linear temperature gradient with respect to the reference spectrum is shown as well. Using the full
260   interferogram, the mean difference shows only little differences across the spectral axis, which shows that the spectrum contains
an averaged temperature information of the given temperatures within the field. Using only the left side of the interferogram
entails that the interferogram contains only temperatures from 190K to 200K. As explained in Sec. 4, lower temperatures
means higher intensities in the central spectral region and lower intensities at the edges of the bandpass filter. Analogously,
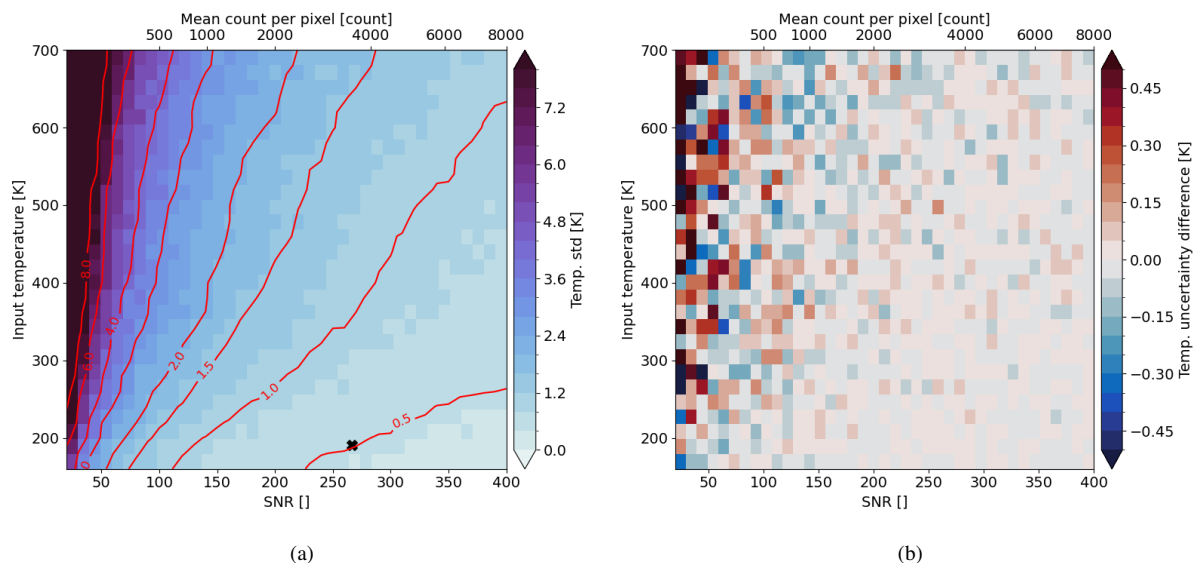
**Figure 9.** (a) Temperature precision of using the right single-sided interferograms assessed for different SNRs and temperatures; (b) difference of temperature precision using the right single-sided interferograms and temperature precision of full interferogram multiplied by $\sqrt{2}$;

the same argument can be applied to the right side of the interferogram. The mean and standard deviation of the retrieved temperatures are shown in Figure 10a. The precision of the temperature retrieval is again decreased by $0.3\mathrm{K} - 0.4\mathrm{K}$. Thus, the decrease in the temperature precision mainly comes from the mirrored shot noise. The retrieved temperatures of the single-sided interferograms lie on average 6K apart of each other, which is closer than the mean temperature of each side suggests. The Fourier transformation maps a weighted sum of all spatial samples in the interferogram to a sample in the spectrum. Thus, the temperature information is localized in the interferogram, but fully distributed across the spectrum. The retrieved temperature is therefore an average of the temperature information within a given region of interest in the interferogram. It should be noted that in the interferogram, intensities that deviate significantly from the mean contribute more to the spectrum. Consequently, these deviations carry a greater amount of temperature information within the spectrum. Thus, the large variations around the ZOPD in the interferogram contribute more to the overall result. Eq. (1) shows that the large variations comes from the fact that the interferogram consists of superimposed cosine waves with zero phase at ZOPD. This is the reason why we did not apply any apodization which applies higher weights to the central region of the interferogram. This will be discussed more in detail in Sec. 5.3.

It is important to acknowledge that the effectiveness of this method relies on accurate knowledge of the ZOPD location. Ntokas et al. (2022) conducted a sensitivity study to assess the impact of the ZOPD location and concluded that precise knowledge of the ZOPD on a sub-pixel scale is necessary to achieve the desired temperature accuracy and precision. Mirroring around the false ZOPD position increases all frequencies on one side and decreases all frequencies on the other side. Failure to

(a)                                    (b)                                    (c)
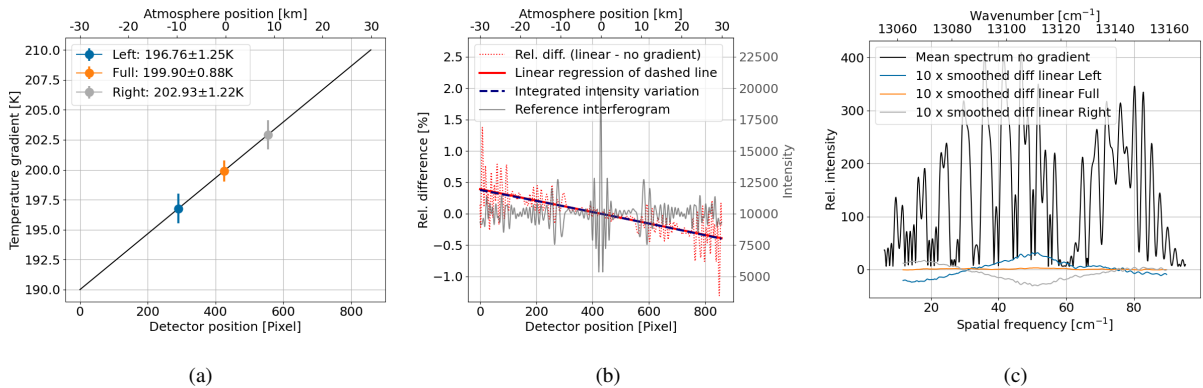
**Figure 10.** Results of Monte-Carlo simulations with 300 samples where shot noise is propagated through the spectrum into the temperature retrieval for an interferogram with a constant temperature at 200K and an interferogram with linear temperature gradient from 190K to 210K; (a) used temperature gradient and retrieved temperatures; (b) reference interferogram (gray line, right y-axis) incorporates a constant temperature at 200K and a mean signal level of 10 000; difference between interferogram with linear temperature gradient and reference interferogram relative to the value 10 000 (mean of interferogram without temperature gradient) including the linear regression of the relative difference (red line, left y-axis); integrated intensity variation within the bandpass filter due to the temperature gradient relative to the intensity corresponding to the central temperature of 200K (blue line, left y-axis); (c) mean of noisy spectra without temperature gradient as reference; mean difference between the noisy spectra incorporating the linear temperature gradient and the reference mean spectrum using full and half-sided interferograms; no apodization is applied;

account for this phenomenon during processing leads to inaccuracies in the temperature estimates. To accurately determine the ZOPD, correction techniques can be employed, which have already been applied to real-world data by Kleinert et al. (2014) and Ungermann et al. (2022). These methods effectively compensate for the interferogram shift by subtracting the linear phase from the spectrum.

## 5.1 Sensitivity to horizontal temperature variations

In this section we assess the sensitivity of the temperature retrieval to horizontal temperature variations. We define a function

$$f : \boldsymbol{T} \mapsto T_{ret} \tag{3}$$

which maps the horizontal temperature variation $\boldsymbol{T}$ to a retrieved average temperature $T_{ret}$. We calculate the derivative of $f$ with respect to $\boldsymbol{T}$ approximated by finite differences. Since the emission has different sensitivities at different background temperatures as shown in Fig. 4, the derivatives are calculated for the whole range of encountered temperatures. The result is shown in Figure 11a. It shows an overall wavy pattern representing changing intensities of emission lines and its modulation through the instrument. The matrix shows that for any temperature level, the retrieved temperature is most sensitive to temperatures close to the main lobe. Figure 11b shows smoothed rows for selected temperature levels of the matrix in Fig 11a. Lower
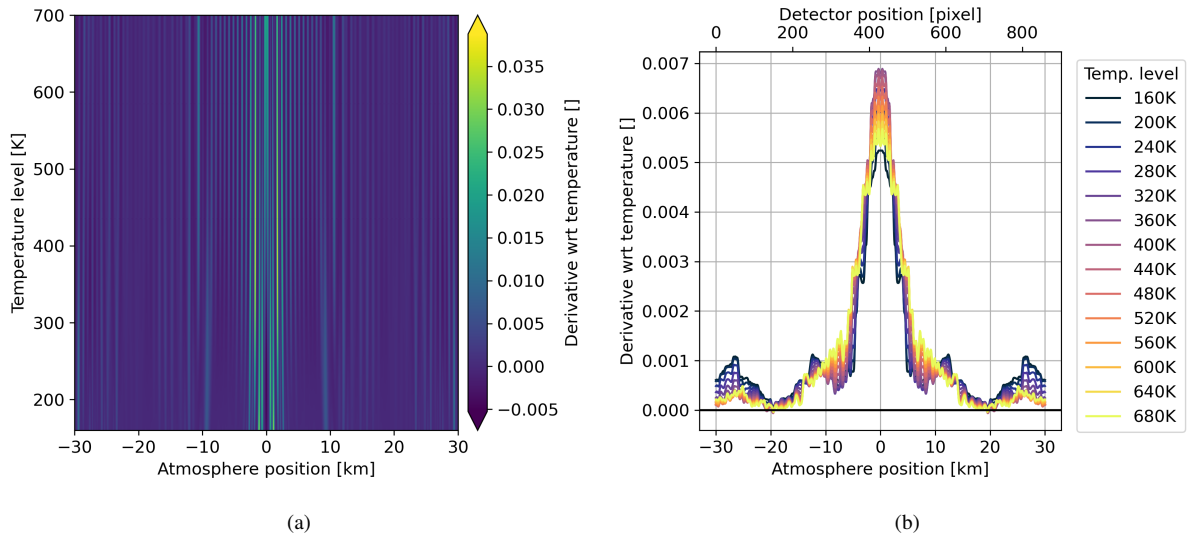
**Figure 11.** (a) Derivative of temperature at a given horizontal position for multiple temperature levels; (b) Selected rows of (a) and smoothed by a running mean with window size 101

temperature below 300K show a lower sensitivity around the main lobe and more sensitivity to the side. Temperature levels around 500K have the highest central peak and the lowest sides. This effect is attenuated for temperatures above 500K. Thus, the temperature retrieval is least sensitive to horizontal temperature variations around 500K. The same effect is seen in Sec. 5.2 and Sec. 5.3.

The Jacobian matrix in Figure 11a can be used in Taylor's theorem to linearly approximate function $f$ defined in Eq. (3). We interpolate the 2-D field and derive the continuous derivative with respect to temperature variation. We split the temperature variation in background and residuals, denoted by $\boldsymbol{T} = \bar{T} + \boldsymbol{T'}$. The retrieved temperature can be then estimated due to Taylor's theorem by

$$\tilde{T}_{ret} = \left(\nabla f(\bar{T}) \cdot \boldsymbol{T'}\right) + \bar{T}, \tag{4}$$

where $\cdot$ denotes the scalar product of two vectors. To put it in context with the linearized diagnostic theory described by Rodgers (2000), the Jacobian of function $f$ is analogous to the averaging kernel matrix which also maps the atmospheric state to the retrieval result. The differences are that the function $f$ maps a vector to a scalar and thus the Jacobian of $f$ is a vector. Further, $f$ and therefore its Jacobian is dependent on the background temperature. The functionality of the presented estimation, however, is similar to the usage of the averaging kernel matrix in a usual retrieval.

To evaluate this approximation we use the simulated temperature variations from Sec. 5.2, estimate the retrieved temperature as explained and compare it to the retrieved temperature running through the entire simulation-processing process explained in Sec. 3.2 and Sec. 3.3. The results are shown in Figure 12, which shows an overall good agreement with 98% being within an error of less than 0.05K. A slight but negligible bias of 0.02K can be seen. The minimal and maximal error is at $-0.10$K and
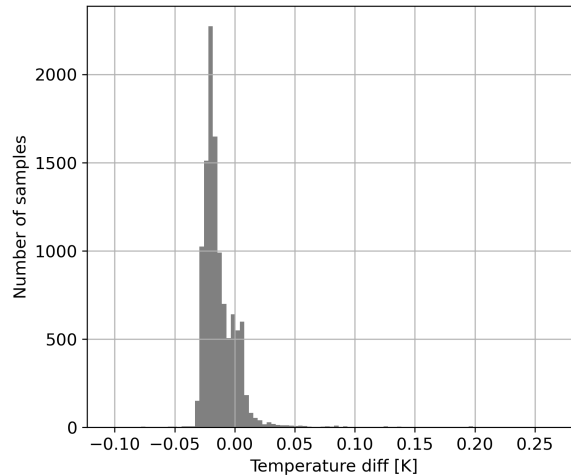
**Figure 12.** Temperature error using derivative matrix from Figure 11a and Eq. (4) to estimate retrieved temperature

0.28K respectively. Thus, the explained method can be used to approximate the retrieved temperature for varying horizontal temperature variations without running through a full end-to-end simulation.

## 5.2 Temperature retrieval of horizontal temperature variations using single-sided interferograms

315 To get a comprehensive picture of the split interferogram processing method, we simulate interferograms according to temperature variations typically produced by gravity waves, split the interferogram and retrieve temperature for each side. When observing temperature variations produced by an atmospheric wave, it is essential to localize that information in space to obtain proper wave characteristics from that data. A sinusoidal horizontal temperature variation can be modelled by

$$\boldsymbol{T} = \bar{T} + A \cos\left(2\pi \frac{\boldsymbol{x}}{\lambda_h} + \phi\right) \tag{5}$$

320 where $\bar{T}$ is the background temperature, $A$ the amplitude, $\lambda_h$ the horizontal wavelength, $\phi$ the phase and $\boldsymbol{x}$ is the horizontal scale. The horizontal field of view is assumed to be $\pm30$km. Following Fig. 2a and 2d, we vary the temperature from 160K to 700K to cover typical low- to mid-latitude conditions. Following Chen et al. (2022), we alter the horizontal wavelength from 200km to 2000km and the amplitude from 4K to 30K. In total, we analysed 4220 simulated temperature variations. Note that temperature variations with a min-max value smaller than 1K are excluded, because they cannot be resolved. For the

325 further analysis we introduce the term 'location' of a retrieved temperature. This is defined by the abscissa of that atmospheric model temperature, which is equal to the retrieved one. The location of the retrieved temperatures of each side relative to the center are shown in Figure 13. Hereby, one parameter is varied while showing the distribution of all waves for the given parameter. Note that the distance between the locations of each side can be seen as a measure for how well the presence of a horizontal temperature variation can be characterized. Figure 13a shows no influence of the amplitude of the temperature
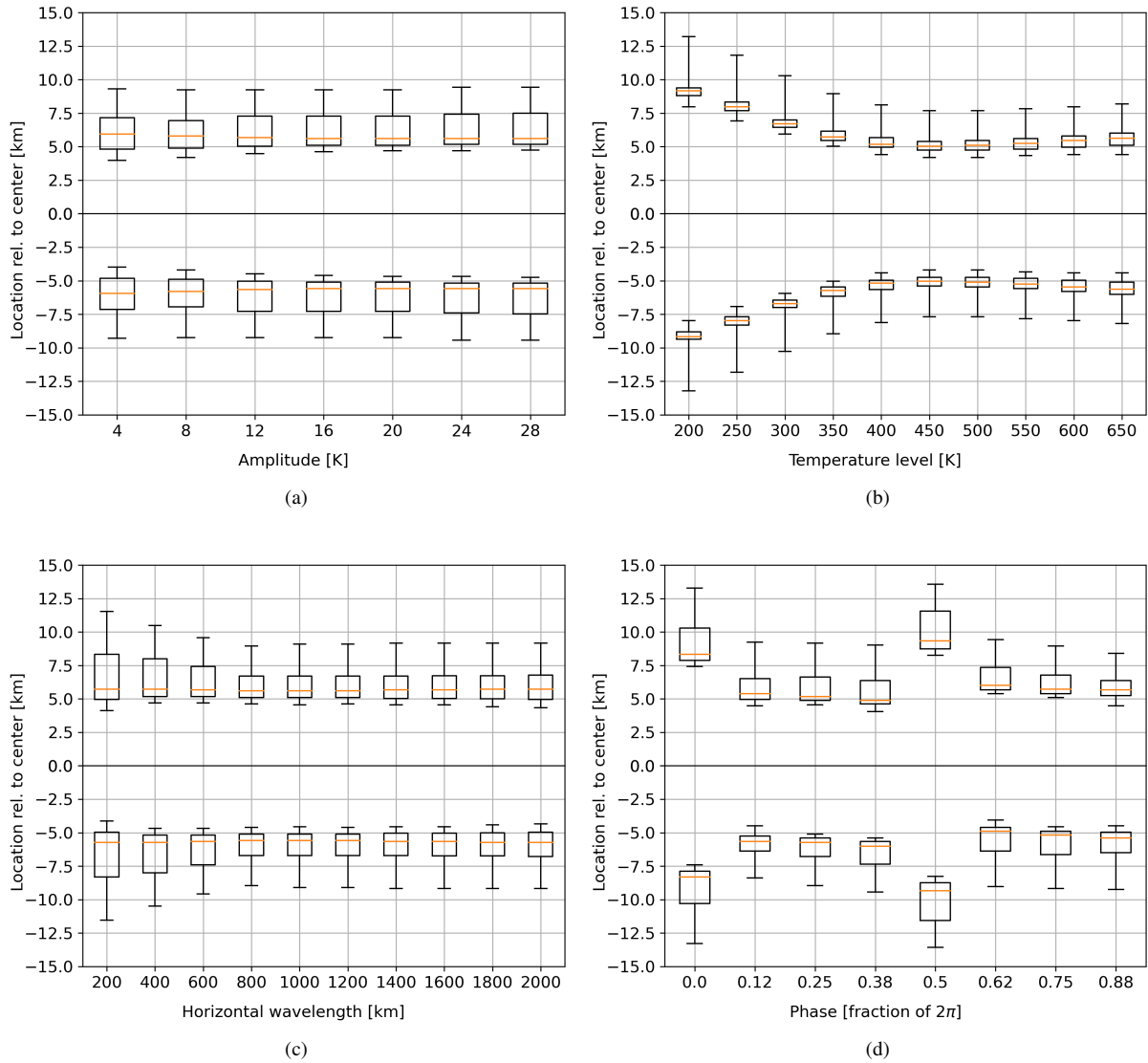
**Figure 13.** Relative location of the retrieved temperatures within the temperature variation using single sided interferograms (a) for varying amplitude, (b) for varying temperature background level, (c) for varying horizontal wavelength and (d) for varying phase; the box extends from the lower to upper quartile values, the whiskers extend from the 5th to 95th percentile;
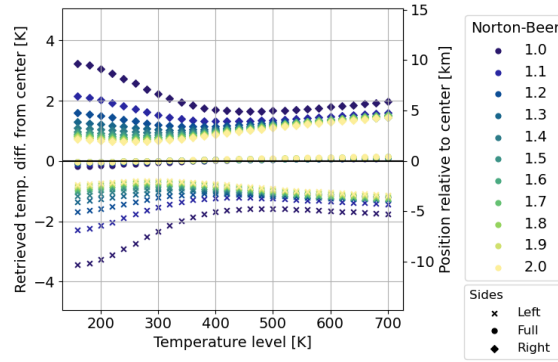
**Figure 14.** Retrieved temperatures using a linear temperature gradient for multiple temperature levels and different strengths of apodization

330  residual onto the location of the retrieved temperatures. Figure 13b shows that the temperature background affects the distance
of the retrieved temperatures due to the different sensitivities of the $O_2$ A-band emission with respect to temperatures. The
results in Sec. 5.1 explains the retrievals of lower temperature having a higher information content at the sides compared to
that of higher temperatures and thus, resulting in retrieved temperatures laying further apart of each other when using single-
sided interferograms. The minimum of this effect is around 500K with a slight increase for temperatures above. The horizontal
335  wavelength of the temperature variation affects only slightly the distance of the retrieved temperature as shown in Figure 13c.
Short wavelengths results in a larger spread of the location distribution due to the fact that the phase of the temperature variation
plays a greater role. When looking at the phase in Figure 13d, $\phi = 0$ and $\phi = \pi$ are outliers referring to the crest and trough of
the captured temperature residual. In both cases, the temperature variation is low within the center and large at the edges. This
works against the increased temperature information around the center and results in temperatures being further apart from
340  each other. To conclude, if one takes the background temperature into account one can give a good estimate of the location of
the retrieved temperature. The effect of the phase will introduce a systematic error at the crest and trough. Compensating these
two effects in the wave analysis, one gets a good estimate of the horizontal wave parameter components.

### 5.3 Apodization

In this section we assess the influence of apodization onto the retrieval of split interferograms. We evaluate this for horizontally
345  linear temperature gradients with a spread of $\pm 10$K for central temperature levels from 160K to 700K and for the Norton-Beer
apodizations introduced in Sec. 3.3. The results are shown in Figure 14. Using the full interferogram the mean temperature
can be recovered for each temperature level independent of the strength of the apodization. Using a single-sided interferogram,
stronger apodization decreases the localization difference between the retrieved temperatures of the left and right side. Revis-
iting Figure 3a the apodization functions decreases the intensity of the interferogram towards the edges and thus put a greater
350  weight on the information content in the central region. The effect that the retrieved temperatures are closer to the center as
explained in Sec. 5.1 is consequently amplified by the apodization function. The case without apodization (Norton-Beer 1.0)

shows a decrease in the temperature difference between the two sides for temperature levels between 160K and 500K and a slight increase for higher temperatures. This shape is consistent with the results shown in Fig. 13b. When using mirrored single-sided interferograms, apodization is not only a trade off between spectral resolution and decrease of the side lobes, but also a trade off between spatial resolution of the two retrieved horizontal temperature data points and robustness against errors (see Sec. 3.3 for link between apodization and robustness). Using single-sided interferograms therefore increases the requirements for instrument error mitigation, if the distance between the two retrieved temperature data points wants to be kept large.

# 6    Conclusions

Spatial heterodyne interferometers are often combined with a two-dimensional focal plane array and a telescope to obtain spatial and spectral information from a scene. This study deals with a limb sounding SHI instrument, which delivers in its default configuration spatial information of the atmosphere in the vertical and spectral information in the horizontal direction across the LOS. However, it is possible to split the interferogram into half to obtain additional spatial information in horizontal direction across the LOS as well. This methodology is firstly applied to spatial heterodyne spectroscopy for atmospheric temperature, which then gives two horizontal temperature profiles (two temperature data points per tangent layer).

This paper first discussed the temperature sensitivity of the captured $O_2$ A-band emission and the resulting temperature precision of the instrument. A special focus is put on the upper limit of resolvable tangent altitudes. To this end, we simulate the expected signal levels for the given instrument specifications and present a temperature precision analysis for different temperatures and signal levels using full interferograms as a baseline simulation. It was shown that the temperature precision is negatively correlated with temperature due to the specific temperature dependence of the emission lines, so that thermospheric temperatures are less precise than mesospheric ones. The simulations show that within the strong emission layer around 90km±10km the temperature precision stays below 1K. During day-time temperatures, altitudes up to 140km can be resolved with either a lower temperature precision or a lower spatial resolution. For example, one would need to bin 60 rows to resolve tangent altitudes around 140km with a temperature precision of 4K. Our analysis does not account for self-absorption, which cannot be neglected for tangent altitudes below 85km. To assess this effect, simulations using a radiative transfer model that includes self-absorption are required.

Further, we show that the method of split interferograms reduces the temperature precision by a factor of $\sqrt{2}$. Analysing the influence of an horizontal temperature variation across the field of view shows that the horizontal localization of retrieved temperatures is generally closer to the center of the field of view. A linearized estimation of the retrieved temperature for a given temperature variation using Taylor's theorem shows that most of the temperature information is localized around the center of the interferogram. Further, it is shown that apodization affects the spatial resolution of the data obtained by this method. In general, weaker apodization gives better spatial resolution across the LOS, which must be balanced against model or instrumental uncertainties. As an application of this method, Chen et al. (2022) showed that medium-scale gravity waves
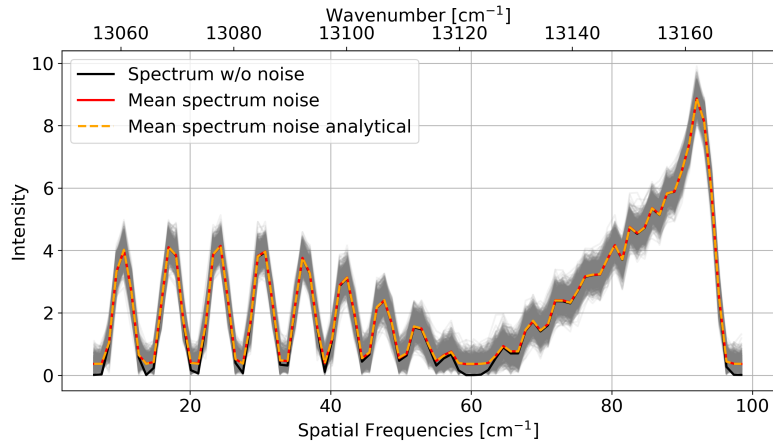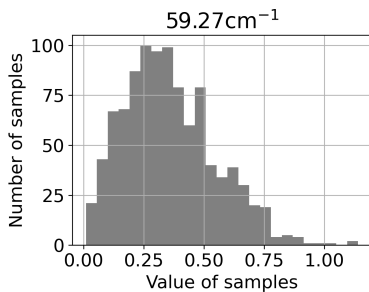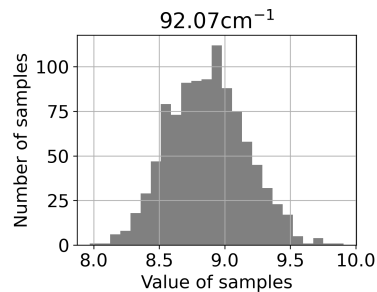
**Figure A1.** (a) Magnitudinal spectra for a low signal with an SNR of 20 and high temperature of 700K with (grey lines) and without (solid black line) shot noise; the mean of the noisy spectra (red solid line) and the analytical mean calculation following the mean of the Rice distribution defined in Eq. (A5) (orange dashed line); (b) and (c) noise distribution at the minimal and maximal spectral sample at $59.27\text{cm}^{-1}$ and $92.07\text{cm}^{-1}$, respectively;

can be horizontally resolved from such data, but it must be taken into account that the phase and background temperature of the captured wave affect the location of the retrieved temperatures.

## Appendix A:  Spectral noise of a magnitudinal spectrum

We can describe the noisy interferogram by

$$\hat{y}[n] = y[n] + \varepsilon[n] \tag{A1}$$

where $\hat{y}$ is the interferogram with noise, $y$ the non-noisy interferogram and $\varepsilon$ the shot noise described by the normal distribution

$$\varepsilon[n] \sim \mathcal{N}(0, \overline{y}) \tag{A2}$$

where $\overline{y}$ is the mean of the signal.

The shot noise can be propagated through the Fourier transformation, resulting in a noisy spectrum given by

$$\text{Re}(\hat{S}[k]) \sim \mathcal{N}(S[k], \frac{\overline{y}}{2N}) \tag{A3}$$

$$\text{Im}(\hat{S}[k]) \sim \mathcal{N}(0, \frac{\overline{y}}{2N}) \tag{A4}$$

where $N$ is the number of samples in the interferogram and $S$ is the non-noisy spectrum. The absolute value of the samples $\sqrt{\text{Re}(\hat{S}[k])^2 + \text{Im}(\hat{S}[k])^2}$ can be described by the Rice distribution (Talukdar and Lawing, 1991), where the distribution in each spectral sample depends on the value of the non-noisy spectral sample. Let $\upsilon = S[k]$ be the mean distance of the real and imaginary part to the origin and let $\sigma = \sqrt{\frac{\overline{y}}{2N}}$ be the standard deviation of the real and imaginary part. The Rice distribution is defined by $\upsilon$ and $\sigma$ and the mean is given by

$$\mu = \sigma \sqrt{\frac{\pi}{2}} {}_1F_1 \left( -\frac{1}{2}; 1; -\frac{\upsilon^2}{2\sigma^2} \right) \tag{A5}$$

where ${}_1F_1$ is the confluent hypergeometric function of the first kind. Note that if apodization is applied, the standard deviation of the noise is decreased.

In Figure A1a we show magnitudinal spectra for a low signal with an SNR of 20 and high temperature of 700K. One can see that the noisy spectra are centered around the non-noisy spectrum for high values but are off for low values. Figure A1c shows that the noise distribution is close to a normal distribution for a high value but skewed for low values as shown in Figure A1b. Within the processing, the deviating mean is subtracted to at least center the noise distribution around the non-noisy spectrum, which reduces the bias. Note that this affects only very low signals which are below the signal levels usually used within the processing.

*Author contributions.* KN performed all simulations and wrote most of the text. JU initiated the analysis regarding the sensitivity to horizontal temperature variations. JU and MK supervised the study. All authors contributed to the discussion of the results, the manuscript review and improvements.

*Competing interests.* At least one of the (co-)authors is a member of the editorial board of Atmospheric Measurement Techniques.

The EMPIR initiative is co-funded by the European Union's Horizon 2020
research and innovation programme and the EMPIR Participating States

*Acknowledgements.* This project 19ENV07 MetEOC-4 has received funding from the EMPIR programme co-financed by the Participating States and from the European Union's Horizon 2020 research and innovation programme.

# References

Alexander, M. J., Geller, M., McLandress, C., Polavarapu, S., Preusse, P., Sassi, F., Sato, K., Eckermann, S., Ern, M., Hertzog, A., Kawatani, Y., Pulido, M., Shaw, T. A., Sigmond, M., Vincent, R., and Watanabe, S.: Recent developments in gravity-wave effects in climate models and the global distribution of gravity-wave momentum flux from observations and models: Recent Developments in Gravity-Wave Effects, Quarterly Journal of the Royal Meteorological Society, 136, 1103–1124, https://doi.org/10.1002/qj.637, 2010.

Barth, C. A. and Hildebrandt, A. F.: The 5577 A airglow emission mechanism, Journal of Geophysical Research, 66, 985–986, https://doi.org/10.1029/JZ066i003p00985, 1961.

Becker, E. and Vadas, S. L.: Explicit Global Simulation of Gravity Waves in the Thermosphere, Journal of Geophysical Research: Space Physics, 125, https://doi.org/10.1029/2020JA028034, 2020.

Bucholtz, A., Skinner, W. R., Abreu, V. J., and Hays, P. B.: The dayglow of the $O_2$ atmospheric band system, Planetary and Space Science, 34, 1031–1035, https://doi.org/https://doi.org/10.1016/0032-0633(86)90013-9, 1986.

Cardon, J., Englert, C., Harlander, J., Roesler, F., and Stevens, M.: SHIMMER on STS-112: Development and Proof-of-Concept Flight, in: AIAA Space 2003 Conference & Exposition, American Institute of Aeronautics and Astronautics, Long Beach, California, https://doi.org/10.2514/6.2003-6224, 2003.

Chen, Q., Ntokas, K., Linder, B., Krasauskas, L., Ern, M., Preusse, P., Ungermann, J., Becker, E., Kaufmann, M., and Riese, M.: Satellite observations of gravity wave momentum flux in the mesosphere and lower thermosphere (MLT): feasibility and requirements, Atmospheric Measurement Techniques, 15, 7071–7103, https://doi.org/10.5194/amt-15-7071-2022, 2022.

Connes, P.: Spectromètre interférentiel à sélection par l'amplitude de modulation, Journal de Physique et le Radium, 19, 215–222, https://doi.org/10.1051/jphysrad:01958001903021500, 1958.

Cooke, B. J., Smith, B. W., Laubscher, B. E., Villeneuve, P. V., and Briles, S. D.: Analysis and system design framework for infrared spatial heterodyne spectrometers, in: Infrared Imaging Systems: Design, Analysis, Modeling, and Testing X, edited by Holst, G. C., pp. 167–191, Proc. SPIE 3701, Orlando, FL, https://doi.org/10.1117/12.352971, 1999.

Englert, C. R., Harlander, J. M., Brown, C. M., Marr, K. D., Miller, I. J., Stump, J. E., Hancock, J., Peterson, J. Q., Kumler, J., Morrow, W. H., Mooney, T. A., Ellis, S., Mende, S. B., Harris, S. E., Stevens, M. H., Makela, J. J., Harding, B. J., and Immel, T. J.: Michelson Interferometer for Global High-Resolution Thermospheric Imaging (MIGHTI): Instrument Design and Calibration, Space Science Reviews, 212, 553–584, https://doi.org/10.1007/s11214-017-0358-4, 2017.

Ern, M.: Absolute values of gravity wave momentum flux derived from satellite data, Journal of Geophysical Research, 109, D20 103, https://doi.org/10.1029/2004JD004752, 2004.

Filler, A. S.: Apodization and Interpolation in Fourier-Transform Spectroscopy, Journal of the Optical Society of America, 54, 762, https://doi.org/10.1364/JOSA.54.000762, 1964.

Florczak, J., Ntokas, K., Neubert, T., Zimmermann, E., Rongen, H., Clemens, U., Kaufmann, M., Riese, M., and van Waasen, S.: Bad pixel detection for on-board data quality improvement of remote sensing instruments in CubeSats, in: CubeSats and SmallSats for Remote Sensing VI, edited by Norton, C. D. and Babu, S. R., p. 3, SPIE, San Diego, United States, https://doi.org/10.1117/12.2633124, 2022.

Gisi, M., Hase, F., Dohe, S., Blumenstock, T., Simon, A., and Keens, A.: $XCO_2$ measurements with a tabletop FTS using solar absorption spectroscopy, Atmospheric Measurement Techniques, 5, 2969–2980, https://doi.org/10.5194/amt-5-2969-2012, 2012.

Gordon, I., Rothman, L., Hargreaves, R., Hashemi, R., Karlovets, E., Skinner, F., Conway, E., Hill, C., Kochanov, R., Tan, Y., Wcisło, P., Finenko, A., Nelson, K., Bernath, P., Birk, M., Boudon, V., Campargue, A., Chance, K., Coustenis, A., Drouin, B., Flaud, J., Gamache,

R., Hodges, J., Jacquemart, D., Mlawer, E., Nikitin, A., Perevalov, V., Rotger, M., Tennyson, J., Toon, G., Tran, H., Tyuterev, V., Adkins, E., Baker, A., Barbe, A., Canè, E., Császár, A., Dudaryonok, A., Egorov, O., Fleisher, A., Fleurbaey, H., Foltynowicz, A., Furtenbacher, T., Harrison, J., Hartmann, J., Horneman, V., Huang, X., Karman, T., Karns, J., Kassi, S., Kleiner, I., Kofman, V., Kwabia–Tchana, F., Lavrentieva, N., Lee, T., Long, D., Lukashevskaya, A., Lyulin, O., Makhnev, V., Matt, W., Massie, S., Melosso, M., Mikhailenko, S., Mondelain, D., Müller, H., Naumenko, O., Perrin, A., Polyansky, O., Raddaoui, E., Raston, P., Reed, Z., Rey, M., Richard, C., Tóbiás, R., Sadiek, I., Schwenke, D., Starikova, E., Sung, K., Tamassia, F., Tashkun, S., Vander Auwera, J., Vasilenko, I., Vigasin, A., Villanueva, G., Vispoel, B., Wagner, G., Yachmenev, A., and Yurchenko, S.: The HITRAN2020 molecular spectroscopic database, Journal of Quantitative Spectroscopy and Radiative Transfer, 277, 107 949, https://doi.org/10.1016/j.jqsrt.2021.107949, 2022.

Gumbel, J., Megner, L., Christensen, O. M., Ivchenko, N., Murtagh, D. P., Chang, S., Dillner, J., Ekebrand, T., Giono, G., Hammar, A., Hedin, J., Karlsson, B., Krus, M., Li, A., McCallion, S., Olentšenko, G., Pak, S., Park, W., Rouse, J., Stegman, J., and Witt, G.: The MATS satellite mission – gravity wave studies by Mesospheric Airglow/Aerosol Tomography and Spectroscopy, Atmospheric Chemistry and Physics, 20, 431–455, https://doi.org/10.5194/acp-20-431-2020, 2020.

Harlander, J., Reynolds, R. J., and Roesler, F. L.: Spatial heterodyne spectroscopy for the exploration of diffuse interstellar emission lines at far-ultraviolet wavelengths, The Astrophysical Journal, 396, 730, https://doi.org/10.1086/171756, 1992.

Johnson, D. G., Traub, W. A., and Jucks, K. W.: Phase determination from mostly one-sided interferograms, Applied Optics, 35, 2955, https://doi.org/10.1364/AO.35.002955, 1996.

Kaufmann, M., Olschewski, F., Mantel, K., Solheim, B., Shepherd, G., Deiml, M., Liu, J., Song, R., Chen, Q., Wroblowski, O., Wei, D., Zhu, Y., Wagner, F., Loosen, F., Froehlich, D., Neubert, T., Rongen, H., Knieling, P., Toumpas, P., Shan, J., Tang, G., Koppmann, R., and Riese, M.: A highly miniaturized satellite payload based on a spatial heterodyne spectrometer for atmospheric temperature measurements in the mesosphere and lower thermosphere, Atmospheric Measurement Techniques, 11, 3861–3870, https://doi.org/10.5194/amt-11-3861-2018, 2018.

Kaufmann, M., Ntokas, K., Sivil, D., Michel, B., Chen, Q., Olschewski, F., Wroblowski, O., Augspurger, T., Miebach, M., Ungermann, J., Neubert, T., Mantel, K., and Riese, M.: Optical Design and Straylight Analyses of a Spatial Heterodyne Interferometer for the Measurement of Atmospheric Temperature from Space, in: CubeSats, SmallSats, and Hosted Payloads for Remote Sensing VII, SPIE, San Diego, United States, submitted, 2023.

Kleinert, A., Friedl-Vallon, F., Guggenmoser, T., Höpfner, M., Neubert, T., Ribalda, R., Sha, M. K., Ungermann, J., Blank, J., Ebersoldt, A., Kretschmer, E., Latzko, T., Oelhaf, H., Olschewski, F., and Preusse, P.: Level 0 to 1 processing of the imaging Fourier transform spectrometer GLORIA: generation of radiometrically and spectrally calibrated spectra, Atmospheric Measurement Techniques, 7, 4167–4184, https://doi.org/10.5194/amt-7-4167-2014, 2014.

Liu, J., Neubert, T., Froehlich, D., Knieling, P., Rongen, H., Olschewski, F., Wroblowski, O., Chen, Q., Koppmann, R., Riese, M., and Kaufmann, M.: Investigation on a SmallSat CMOS image sensor for atmospheric temperature measurement, in: International Conference on Space Optics — ICSO 2018, edited by Karafolas, N., Sodnik, Z., and Cugny, B., p. 237, SPIE, Chania, Greece, https://doi.org/10.1117/12.2536157, 2019.

Naylor, D. A. and Tahic, M. K.: Apodizing functions for Fourier transform spectroscopy, Journal of the Optical Society of America A, 24, 3644, https://doi.org/10.1364/JOSAA.24.003644, 2007.

Norton, R. H. and Beer, R.: New apodizing functions for Fourier spectrometry, Journal of the Optical Society of America, 66, 259, https://doi.org/10.1364/JOSA.66.000259, 1976.

Ntokas, K., Kaufmann, M., Ungermann, J., Preusse, P., and Riese, M.: Retrieval of gravity wave parameters using half interferograms measured by CubeSats, in: CubeSats and SmallSats for Remote Sensing VI, edited by Norton, C. D. and Babu, S. R., p. 9, SPIE, San Diego, United States, https://doi.org/10.1117/12.2633460, 2022.

Ortland, D. A., Hays, P. B., Skinner, W. R., and Yee, J.-H.: Remote sensing of mesospheric temperature and $O_2(^1\Sigma)$ band volume emission rates with the high-resolution Doppler imager, Journal of Geophysical Research: Atmospheres, 103, 1821–1835, https://doi.org/10.1029/97JD02794, 1998.

Poghosyan, A. and Golkar, A.: CubeSat evolution: Analyzing CubeSat capabilities for conducting science missions, Progress in Aerospace Sciences, 88, 59–83, https://doi.org/10.1016/j.paerosci.2016.11.002, 2017.

Rodgers, C. D.: Inverse Methods for Atmospheric Sounding: Theory and Practice, vol. 2 of *Series on Atmospheric, Oceanic and Planetary Physics*, WORLD SCIENTIFIC, https://doi.org/10.1142/3171, 2000.

Schmidt, H., Brasseur, G. P., Charron, M., Manzini, E., Giorgetta, M. A., Diehl, T., Fomichev, V. I., Kinnison, D., Marsh, D., and Walters, S.: The HAMMONIA Chemistry Climate Model: Sensitivity of the Mesopause Region to the 11-Year Solar Cycle and $CO_2$ Doubling, Journal of Climate, 19, 3903–3931, https://doi.org/10.1175/JCLI3829.1, 2006.

Sheese, P.: Mesospheric ozone densities retrieved from OSIRIS observations of the oxygen A-band dayglow, Ph.D. thesis, Library and Archives Canada, Ottawa, iSBN: 9780494649367 OCLC: 1006830307, 2009.

Smith, B. W. and Harlander, J. M.: Imaging spatial heterodyne spectroscopy: theory and practice, in: Infrared Technology and Applications XXV, edited by Andresen, B. F. and Strojnik, M., p. 925, Proc. SPIE 3698, Orlando, FL, https://doi.org/10.1117/12.354497, 1999.

Song, R., Kaufmann, M., Ungermann, J., Ern, M., Liu, G., and Riese, M.: Tomographic reconstruction of atmospheric gravity wave parameters from airglow observations, Atmospheric Measurement Techniques, 10, 4601–4612, https://doi.org/10.5194/amt-10-4601-2017, 2017.

Talukdar, K. K. and Lawing, W. D.: Estimation of the parameters of the Rice distribution, The Journal of the Acoustical Society of America, 89, 1193–1197, https://doi.org/10.1121/1.400532, 1991.

Triplett, C. C., Harding, B. J., Wu, Y.-J. J., England, S., Englert, C. R., Makela, J. J., Stevens, M. H., and Immel, T.: Large-Scale Gravity Waves in Daytime ICON-MIGHTI Data from 2020, Space Science Reviews, 219, 3, https://doi.org/10.1007/s11214-022-00944-w, 2023.

Ungermann, J., Kleinert, A., Maucher, G., Bartolomé, I., Friedl-Vallon, F., Johansson, S., Krasauskas, L., and Neubert, T.: Quantification and mitigation of the instrument effects and uncertainties of the airborne limb imaging FTIR GLORIA, Atmospheric Measurement Techniques, 15, 2503–2530, https://doi.org/10.5194/amt-15-2503-2022, 2022.

Vincent, R. A.: The dynamics of the mesosphere and lower thermosphere: a brief review, Progress in Earth and Planetary Science, 2, 4, https://doi.org/10.1186/s40645-015-0035-8, 2015.

Watchorn, S., Roesler, F. L., Harlander, J. M., Jaehnig, K. P., Reynolds, R. J., and Sanders III, W. T.: Development of the spatial heterodyne spectrometer for VUV remote sensing of the interstellar medium, in: UV/EUV and Visible Space Instrumentation for Astronomy and Solar Physics„ edited by Siegmund, O. H. W., Fineschi, S., and Gummin, M. A., pp. 284–295, Proc. SPIE 4498, San Diego, CA, https://doi.org/10.1117/12.450063, 2001.

Yankovsky, V. and Vorobeva, E.: Model of Daytime Oxygen Emissions in the Mesopause Region and Above: A Review and New Results, Atmosphere, 11, 116, https://doi.org/10.3390/atmos11010116, 2020.

Zarboo, A., Bender, S., Burrows, J. P., Orphal, J., and Sinnhuber, M.: Retrieval of $O_2(^1\Sigma)$ and $O_2(^1\Delta)$ volume emission rates in the mesosphere and lower thermosphere using SCIAMACHY MLT limb scans, Atmospheric Measurement Techniques, 11, 473–487, https://doi.org/10.5194/amt-11-473-2018, 2018.